Part 6

Mesoscale organization of IOP 12 Cloud System

by
Yvon Lemaître,
Alain Protat,
and Dominique Bouniol

Centre d'étude des Environnements Terrestre et Planétaires, CNRS, Vélizy, France.

6.1 Synoptic overview of IOP 12

Let us first give an overview of the synoptic context and main characteristics associated with the FASTEX IOP12. A quick-look summary is shown in section 3.15 of Part 3, page 112 of this Report. The whole of February was characterized by a very stable zonal regime. During this month, the wind at 300 mb was on average 10 ms^{-1} stronger than its climatological value (Joly et al. 1999).

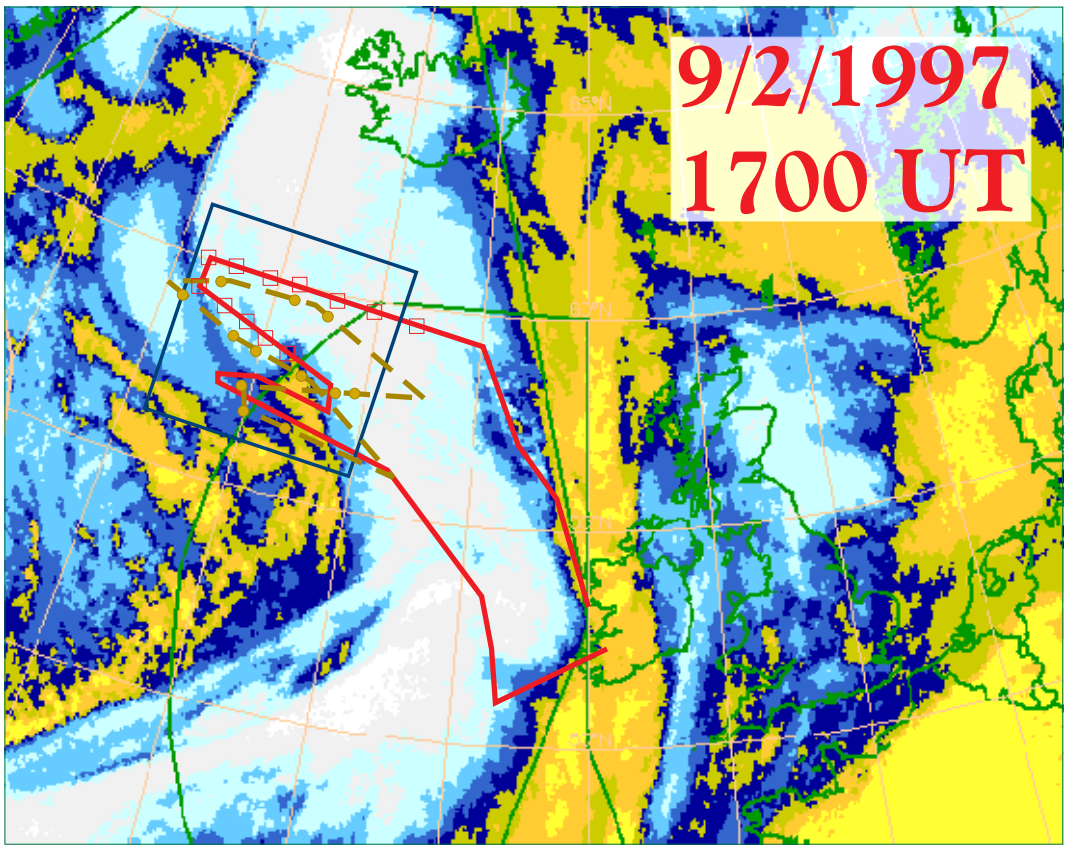

Figure 6.1: *METEOSAT infrared image at 1700UTC. The trajectories of the P3 and C-130 aircraft (red solid and brown dashed lines, respectively) are also displayed in the moving frame relative to the cyclone motion. Boxes correspond to the locations of the regular circular trajectories performed by the P3 aircraft. The mesoscale domain in which the 3D wind and precipitation fields are retrieved is also shown as a large rectangle. Image courtesy of Eumetsat and processed by Météo-France.*

The IOP 12 was conducted on Low 34A, which underwent on 9 February 1997 the most explosive deepening of the period, roughly −54 mbar in 24 hours. This very rapid development is illustrated on the METEOSAT images in the infrared channel shown on Fig. 2.3 in Part 2. Between 06 and 12 UTC, Low 34A moved northeastwards at a fast speed of 40 ms^{-1}. Subsequently, the cyclone deepened very rapidly as it turned to the north just after it crossed the upper-level jet, and tracked towards Iceland, traversing the northwestern corner of the MSA. This Low, which marked the

end of the first most active portion of the zonal regime, was preceded by numerous active systems. It appeared to interact with Low 31 and with the cold air which had been previously advected eastwards by Low 32 (an arctic vortex centered near 62°N, 55°W). Chaigne (1998) also showed, using the potential vorticity inversion technique, that when removing the upper-level feature Low 34A does not develop, which suggests the importance for rapid deepening of a baroclinic interaction process between two independent precursors, one in the lower troposphere and the other at the tropopause.

6.2 Mesoscale measurements collected in the MSA

The documentation of the mesoscale dynamic structure of the cyclone is conducted in the present paper using the MSA facilities. We will focus more precisely at the end of the life cycle of the cyclone, corresponding to the last panel of Fig. 2.3 in Part 2 reproduced here as Fig. 6.1. Among the numerous instruments involved in this experiment, the P3-43 airborne Doppler radar instrumented with a C-band lower fuselage non-Doppler radar and the dual-beam X-band Doppler radar designed at the CETP (mounted on the tail of the aircraft) gathered Doppler informations within this particularly impressive secondary cyclone, using a new sampling strategy defined for FASTEX. An example of raw radar data showing one of the features discussed later in the text is shown on Fig. 6.2.

This strategy consists of a systematic, regular survey (called the "lawnmover" or "systematic survey" pattern) using straight-line flight patterns (called "legs"). The P3 and C-130 aircraft flew parallel legs spaced about 100 km apart, providing a continuous radar coverage and regularly-spaced dropsonde-derived vertical profiles relative to the whole wave cyclone from front to rear (with respect to cyclone motion). The leg length are about 500 km long accross the system and perpendicular to the cyclone motion vector, with at regular interval complete 360°turns. This type of scanning allows for the recovery of vertical profiles of crucial kinematic parameters, such as the terminal fall velocity V_f of hydrometeors, as shown by Protat et al. (1997) and Scialom et al. (1999). The technique employed in this case and the related results are presented in Part 5 on this Report for the same case study.

In the present part, the 3-D wind field is recovered inverting the Doppler measurements collected during the IOP 12 "lawnmover" pattern using the MANDOP technique (Scialom and Lemaître 1990; Dou et al. 1996). The dynamic perturbations (pressure and temperature, essentially) are retrieved under an analytical form, by introducing the analytical form of the 3-D wind field in the non-dissipative and stationary first-order anelastic approximation of the equation of motion (Protat et al. 1998).

6.3 Structure and features of the Cloud System

The purpose of this section is to document the mesoscale dynamics of the secondary cyclone sampled during the IOP 12 of FASTEX. Fig. 6.1 shows the METEOSAT infrared picture at 1700 UTC. It gives the cloud cover associated with the frontal system along which the secondary cyclone develops. Several features are well recognized :

(i) a well-defined frontal cloud band, generally associated with the synoptic warm conveyor belt (WCB, Harrold 1973),

Figure 6.2: *Example of raw radar data obtained from the lower fuselage radar of the NOAA-P3 aircraft, showing the cloud system around 1600UTC, this image being an average over 20′. These images are available in real time during the flight and they are used to adjust the flight plan when this is needed. On this particular image, the maximum of reflectivity that can be seen near the lower right corner is feature A of Fig. 6.3. Image courtesy of Dave Jorgensen, NOAA/NSSL.*

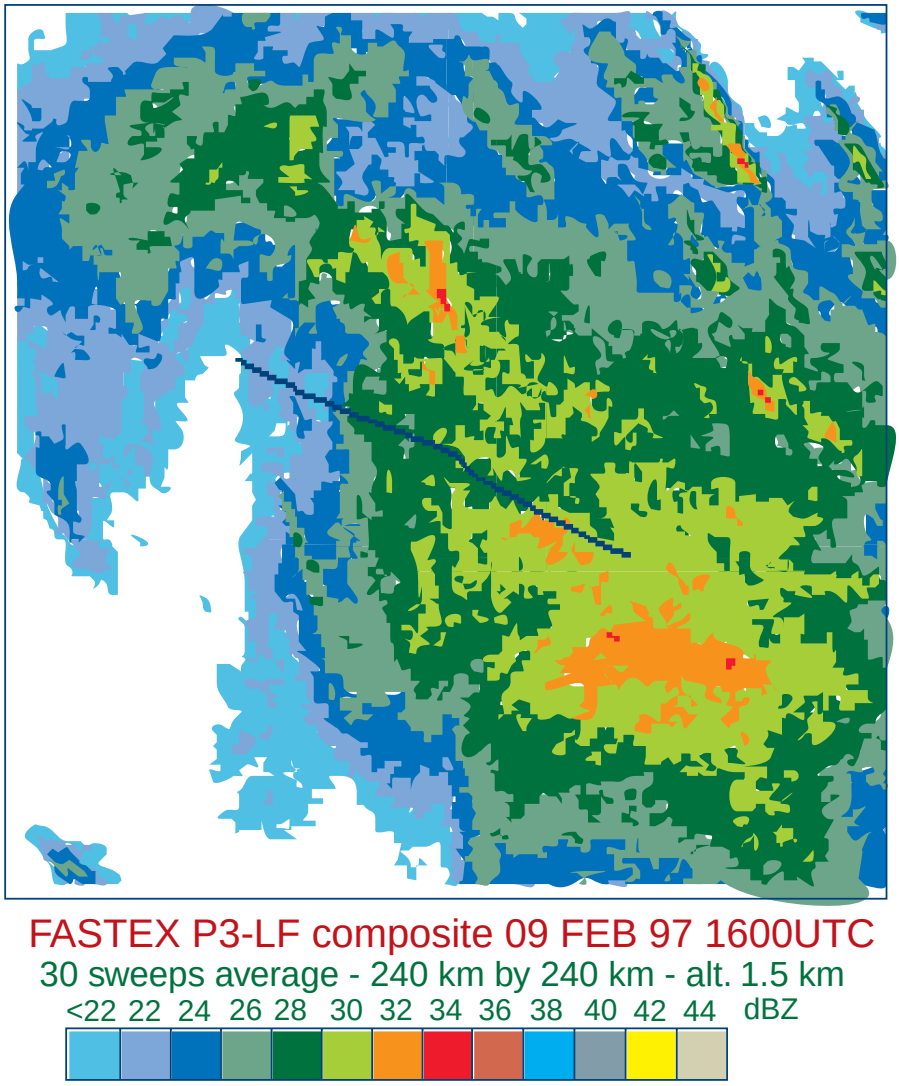

(ii) a well-developed "cloud head" (Bottger et al. 1975) to the northeast of the main baroclinic zone cloud band, the apparition of which is a well-known symptom of cyclogenesis (e. g., Browning and Roberts 1994),

(iii) a dry slot forming between the main baroclinic zone cloud band and the cloud head indicative of a dry intrusion (Reed and Danielsen 1959) of air coming from the upper-troposphere towards the centre of a developing cyclone, and

(iv) the existence of scattered clouds associated with the cold polar air propagating over the sea.

In Fig. 6.1 are also given the trajectories performed by the P3 (solid line) and C-130 (dashed line) aircraft within the secondary cyclone. These trajectories are relative to the cyclone phase speed. The measurements collected by the Doppler and dropsonde facilities along these trajectories allow to retrieve 3-D fields in the mesoscale domain ($430\times430\times7$ km^3) indicated by the box of Fig. 6.1. Fig. 6.3a is a zooming view of the satellite picture of Fig. 6.1 in the vicinity of this mesoscale domain, with upper clouds contoured. This figure can be compared with the 3-D precipitation field derived from the processing of the tail-radar measurements, which is given in Fig. 6.3b on a horizontal cross-section at the flight altitude (roughly 1.5 km). Superimposed to this horizontal cross-section of precipitation are the trajectory of the P3 aircraft and the flight-level in-situ horizontal wind measurements. On the satellite picture (Fig. 6.3a), several upper cloud features are well identified. Within the edge of the main baroclinic zone cloud band appear three distinct upper level features referred to as I, II, and III, respectively, in Fig. 6.3a. These features are associated with the cold frontal surface (features II and III), and likely with the presence of a warm frontal surface (feature I). The warm frontal feature could result from the ascent of the WCB over a cold conveyor belt, a configuration that is often observed during the life cycle of an occlusion (e. g., Carlson 1980; Neiman and Shapiro 1993; Browning and Roberts 1994; L98).

The cloud head itself, located in the mesoscale domain, is characterized by two main upper cloud regions (with a lesser vertical extent, denoted A and B in Fig. 6.3a). The precipitation field of Fig. 6.3b exhibits a large area of precipitation along the northern part of the domain within the main baroclinic zone cloud band. The cloud head is characterized by two main comma-shaped precipitating areas, separated by a transition region of lighter precipitation. These two comma-shaped regions are closely related to the upper cloud features A and B observed on the satellite picture of Fig. 6.3a. The most intense comma-shaped area wraps around a clear-air region, denoted DS in the following, corresponding to the northernmost part of the dry slot. The southernmost precipitating area (only a part of which is sampled by the Doppler radar, see Fig. 6.3b) is correlated with the southeastern part of the large cloudy area located southwest of the cloud head (Fig. 6.3b).

This comparison between cloud cover and radar-derived precipitation evidences that precipitation is not homogeneously distributed inside the cloud head, but rather distributed *along the border of the cloud head*. This suggests that distinct dynamical characteristics may be acting within the various precipitating features of the cloud head. The in-situ horizontal wind measurements in the ground-relative frame (Fig. 6.3b) confirm the link between the most active part of the cloud head (region A in Fig. 6.3) and the WCB (roughly 35 ms^{-1} at the 1.5 km altitude). They also evidence two different dynamical characteristics, associated respectively with the main baroclinic zone cloud band (strongest winds on the right-side) and with the cloud head (weaker winds on the left side).

Finally, a southwesterly airflow is detected in the dry slot area, which likely corresponds to the well-known dry intrusion of upper-tropospheric air approaching the cyclone center (e. g., Reed and Danielsen 1959; Green et al. 1966; Young et al. 1987).

6.4 3-D kinematics retrieved from the Doppler radar

We now turn to a description of the 3-D kinematic fields derived from the Doppler measurements using the MANDOP technique (Scialom and Lemaître 1990; Dou et

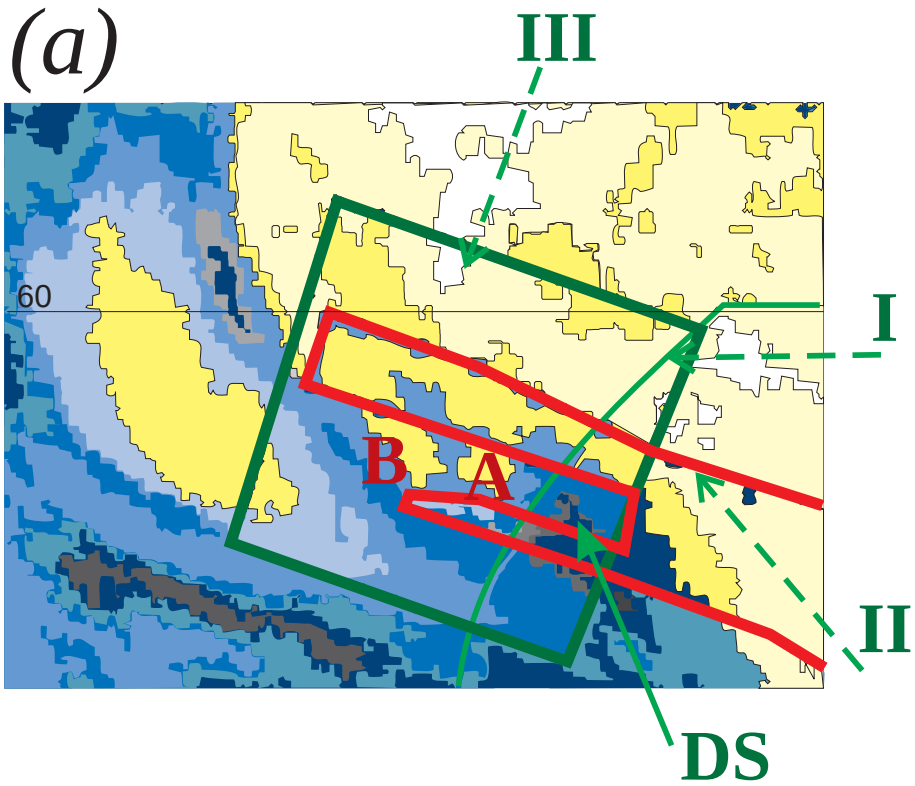

Figure 6.3: *(a) zooming view of Fig. 6.1 in the vicinity of the mesoscale domain (large rectangle), with the upper-clouds contoured and (b) horizontal cross-section of the 3D radar reflectivity field deduced from the tail-radar measurements at the flight-level altitude (1.5 km) within the mesoscale domain of Fig. 6.3a. The respective locations of the features I, II, III, A, B and DS discussed in the text are also given. As usual, brighter shading corresponds to higher clouds (that is, lower brightness temperatures). Arrows in Fig. 6.3 are the in-situ horizontal wind measurements collected at the flight-level altitude (1.5 km).*

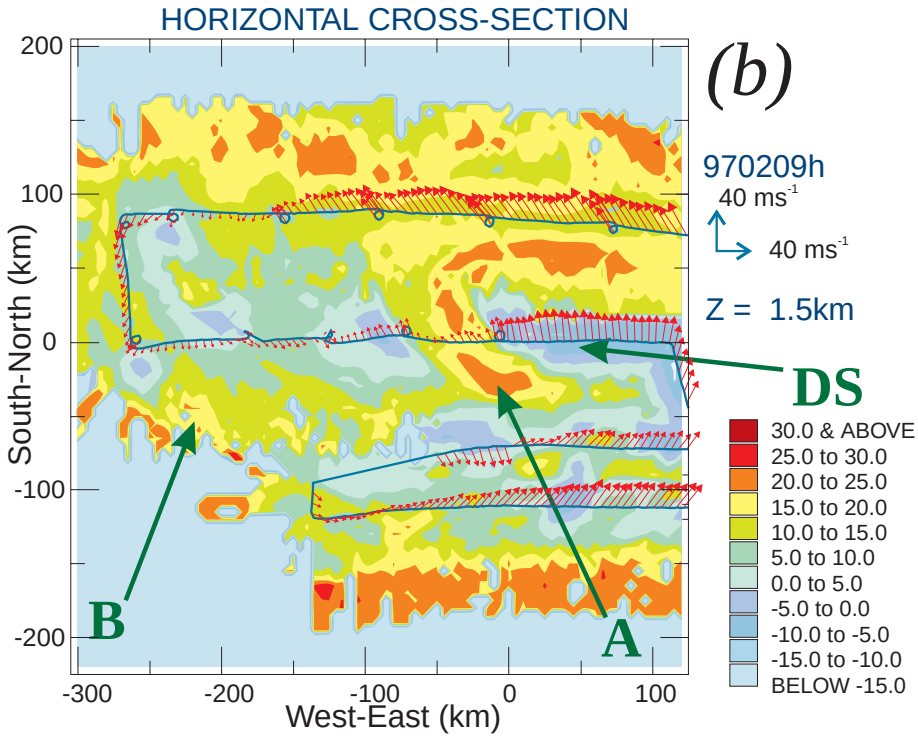

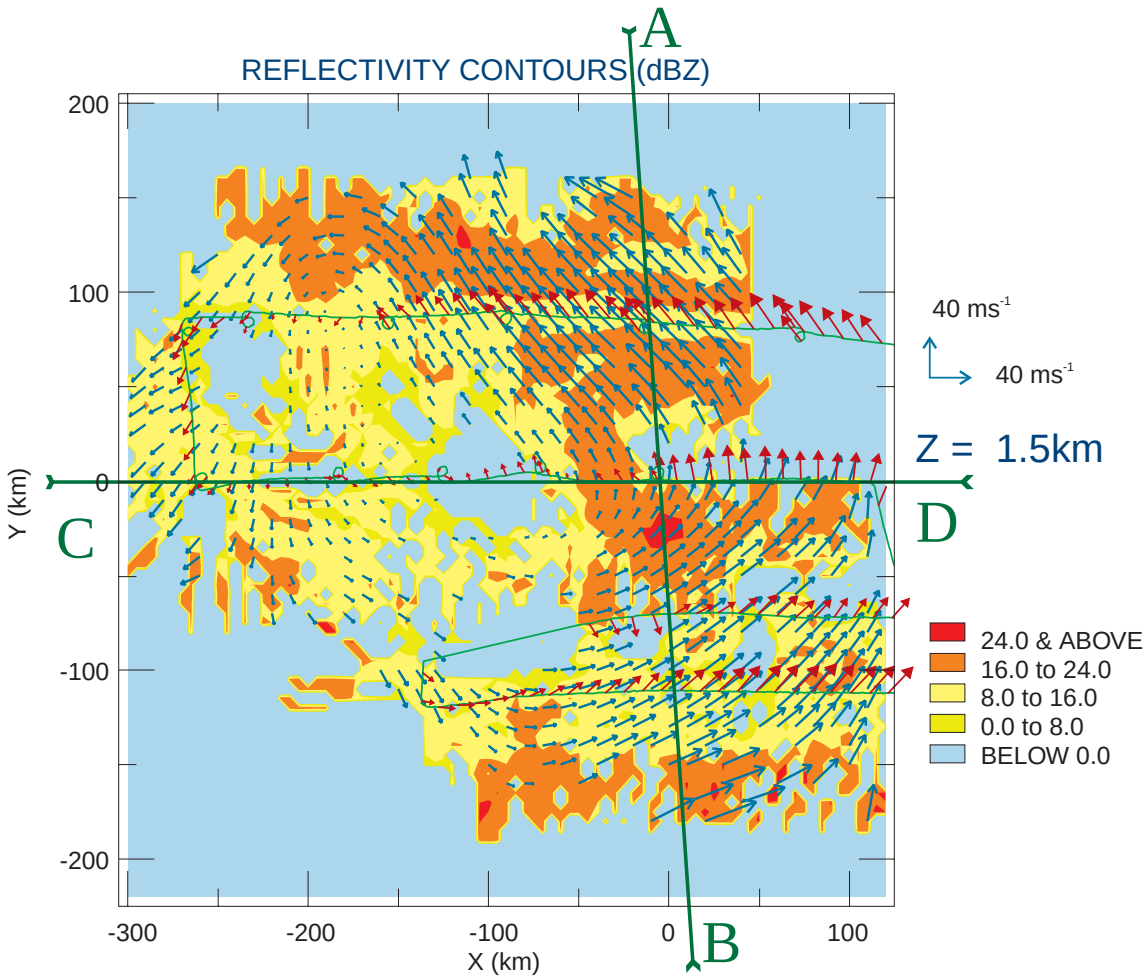

Figure 6.4: *Horizontal cross-section of the 3D radar reflectivity and absolute wind fields at the 1.5-km altitude. Superimposed along the P3-trajectory are the in-situ horizontal wind measurements collected at the flight-level altitude (arrows with solid head). For display purposes, one arrow out of ten is drawn for the in-situ measurements, and one arrow out of two for the retrieved horizontal wind vectors. Also given are the locations in the mesoscale domain of the vertical cross-sections (AB) and (CD) of Fig. 6.6.*

al. 1996). Fig. 6.4 shows the horizontal cross-section of the 3-D precipitation and absolute wind fields at the 1.5-km altitude, with the in-situ measurements of horizontal wind superimposed. First, notice the good agreement between the retrieved and in-situ horizontal winds. The retrieved horizontal wind confirms the existence of the southeasterly flow (WCB) in the region of strong precipitation located in the northeastern part of the domain. It also shows that the region of lighter precipitation corresponds in terms of dynamics to the transition zone between this WCB and the diffluent northeasterly flow located in the western part of the domain. The same 3-D fields are now shown in a frame relative to the cyclone motion and at the 0.5- and 2.5-km altitude (Figs. 6.5a and 6.5b, respectively).

Globally, the same kinematic characteristics are found at both altitudes, except in the northeastern part of the domain, where the easterly relative airflow at the

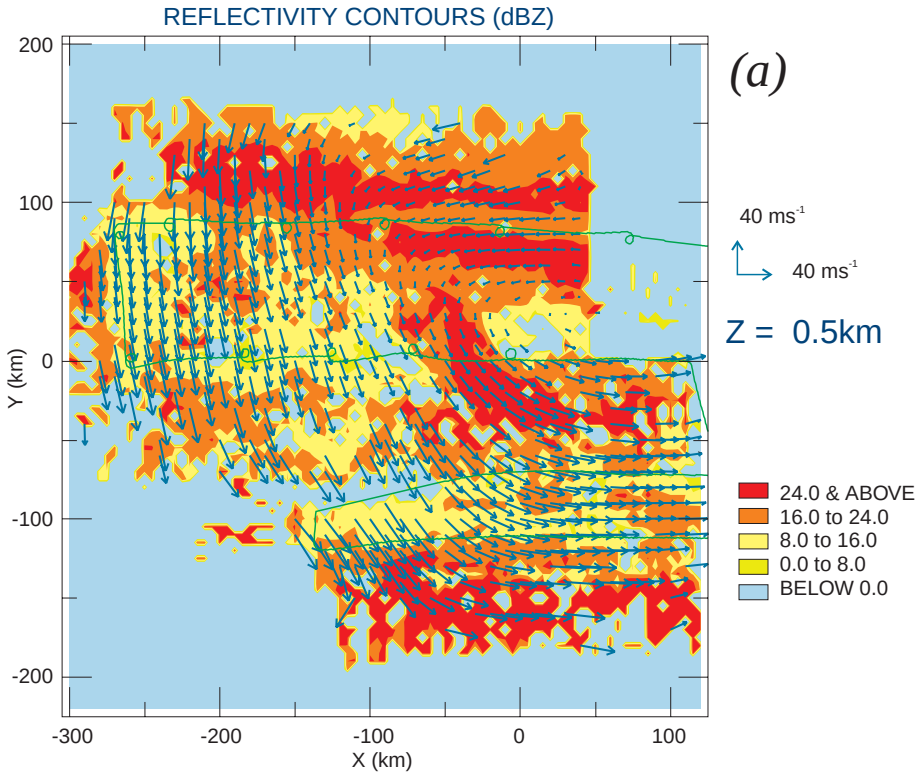

Figure 6.5: *Horizontal cross-section of the 3D radar reflectivity and relative wind fields at the (a)0.5- and (b)-2.5 km altitude.*

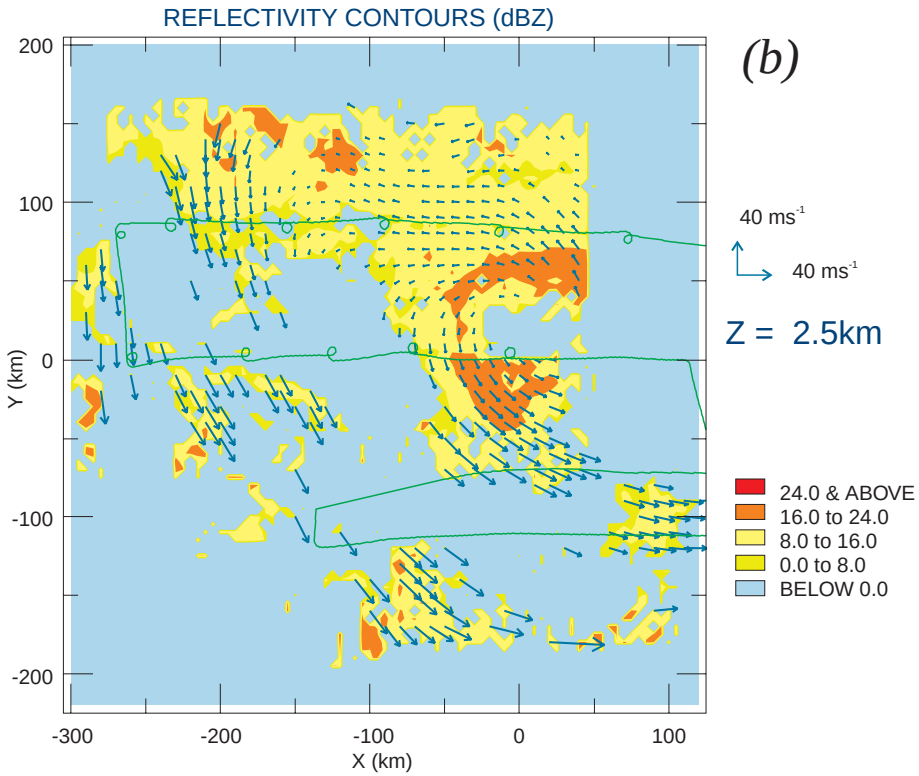

2.5-km altitude (corresponding to the WCB) is found to penetrate further west with height, suggesting an overlapping of the northerly flow by the WCB. A more precise inspection of this easterly relative airflow reveals at the 0.5-km altitude (Fig. 6.5a) the existence of two distinct flows that enter in confluence. The southernmost flow corresponds to the lower part of the WCB, while the northernmost flow could be, according to the conceptual scheme proposed by Browning and Roberts (1994, 1996), the signature of a cold conveyor belt. This lower part of the WCB (denoted W2 in the following so as to keep consistency with the notations of Browning and Roberts 1994) appears to wrap around the most active part A (in terms of precipitation) of the cloud head, suggesting that W2 peels off from the base of the WCB to feed the upper part of the cloud head, as first introduced by Young et al. (1987), developed by Young (1989), and diagnosed recently using numerical models (e. g., Browning and Roberts 1994). The importance of this "peeling-off" process will be confirmed observationally in the following using vertical cross sections through the cloud head and air parcel trajectory analysis.

Such a vertical cross-section through the main entities of this cyclone (the cold conveyor belt, the most active part of the cloud head, and the dry slot) is given in Fig. 6.6. It is seen from the radar reflectivity of Fig. 6.6a that the maximum depth of the reflectivity echoes within the whole cloud head (6 km) is associated with its most active part, which is consistent with the upper clouds located here on the satellite picture of Fig. 6.3a. The depth of the convective cells associated with the southeastern part of the large cloudy area located southwest of the could head (Fig. 6.3b) does not exceed 2 km. The precipitating area located on the northernmost part of the domain results from ascending motions initiated at low levels where W2 overlaps the cold conveyor belt.

6.5 Air trajectories

An air parcel trajectory illustrating these ascending motions is given in Fig. 6.7a. It shows that low-level air parcels are advected along the main baroclinic zone cloud band while rising, corresponding to a vertical transport to the northwest of low-level potential energy. Whether this parcel is part of the cold conveyor belt or of W2 cannot be assessed unambiguously, given the horizontal scale resolved by the mesoscale analysis in the present case. This point will be addressed in future works by performing higher-resolution 3-D wind field retrieval in a convective-scale domain focussing on this particular area.

Interestingly, the shape of these rising trajectories (see in particular the projection of the trajectory of Fig. 6.7a onto the horizontal plane) explains the southwestward limit of stronger precipitation associated with this ascending flow. In contrast, precipitation within the most active part A of the cloud head are associated with ascending motions present at higher altitude (above 2.5 km altitude, see Fig. 6.6a). The air parcel trajectory analysis reveals that these motions are fed by air parcels located initially within W2. An air parcel trajectory representative of these motions, given in Fig. 6.7b, shows effectively that the precipitation area A (Fig. 6.3) within the cloud head results from the slantwise ascent of W2, which wraps around the clear-air region DS. The vertical cross-section of Fig. 6.6a also reveals the existence of descending motions in the dry slot area, as expected from previous studies (e. g., Reed and Danielsen 1959; Green et al. 1966; Young et al. 1987). A better 3-D view of this descending flow is shown by the air parcel trajectory given in Fig. 6.7c.

Figure 6.6: *Vertical cross-section through the mesoscale domain of wind along the plane of the cross-section and (a) radar refelctivity along cross-section (AB) of Fig. 6.4, (b) vertical component of vorticity along cross-section (CD) of Fig. 6.4, taken roughly perpandicular to (AB).*

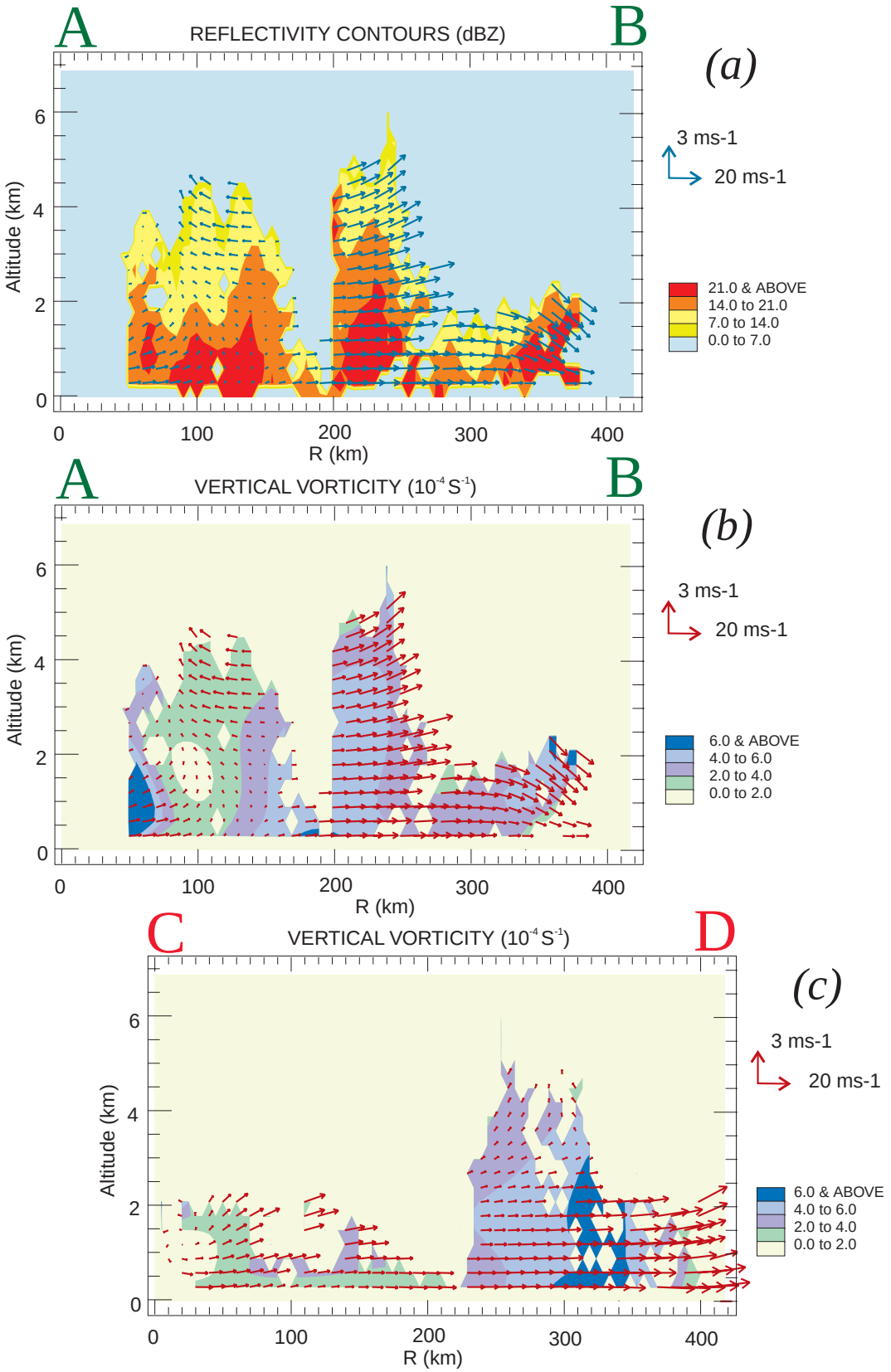

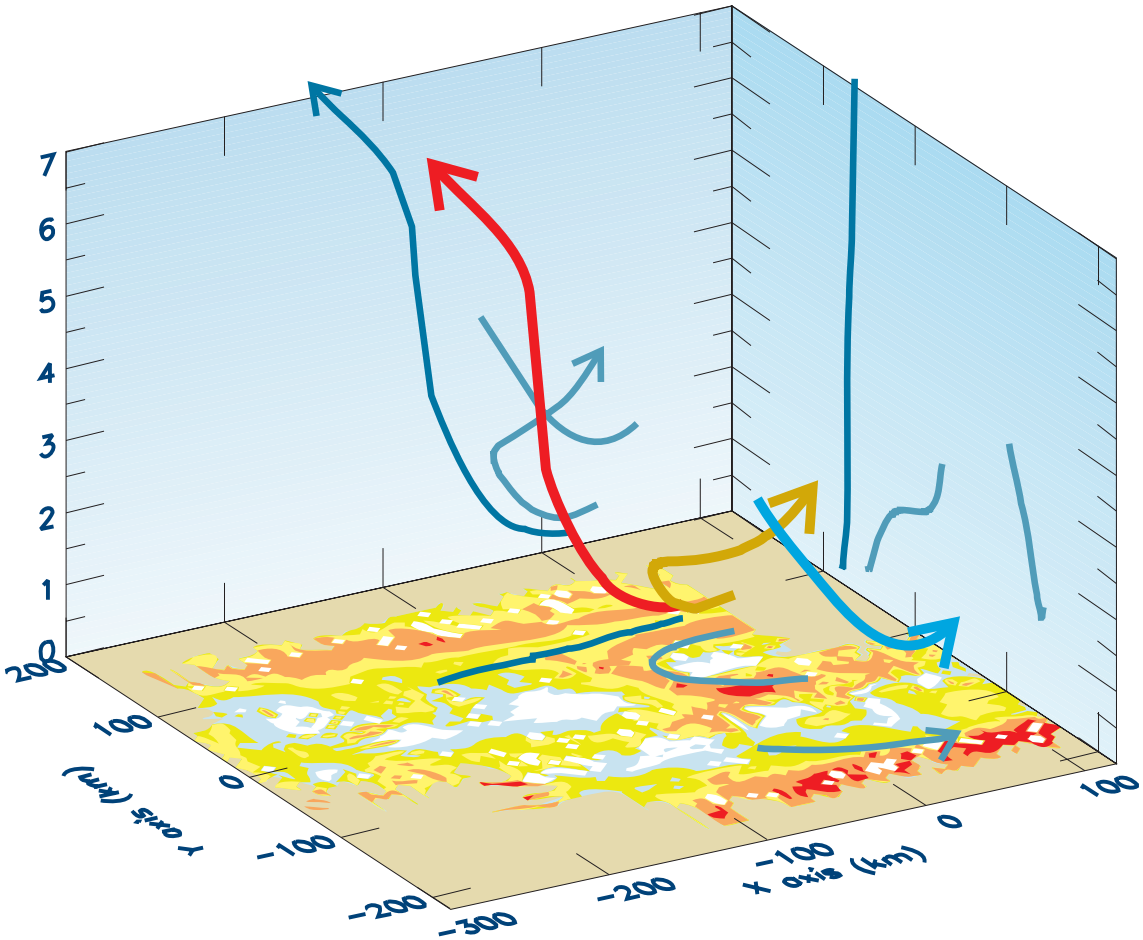

Figure 6.7: *Air parcel trajectories representative of (a) the air rising along the northernmost precipitating area associated with the frontal cloud band (red stream), (b) the W2 airflow wrapping around the most active part of the cloud head (sandy stream, a region of Fig. 6.3c), (c) the southernmost part of the dry intrusion (blue stream).*

Although the second comma-shaped precipitation structure (denoted B in Fig. 6.3) is not well sampled by the Doppler radar, some valuable information can be gained using the air parcel trajectory analysis about the difference in precipitation intensity between B and the region of lighter precipitation located between A and B. It appears indeed that the westernmost air parcel (Fig. 6.8a) rises more vertically than the easternmost one (Fig. 6.8b) although these two regions are fed by the same airflow (see Figs. 6.8a,b). In any case, the parcels associated with the B region seem to originate at low levels rather than at upper levels, which is not a common feature (to our knowledge) found in previous studies. This suggests that this part of the cloud head could result from the release of convective instability during the propagation of the northeasterly flow in the western part of the domain above the warmer ocean (see for instance the recent simulations of Vallis et al. 1997). This aspect will be further studied using convective-scale retrievals of the 3-D dynamic fields.

The vertical component of vorticity (referred to as the "vertical vorticity" in the following) in the same vertical cross-section as Fig. 6.6a (Fig. 6.6b) shows the exis-

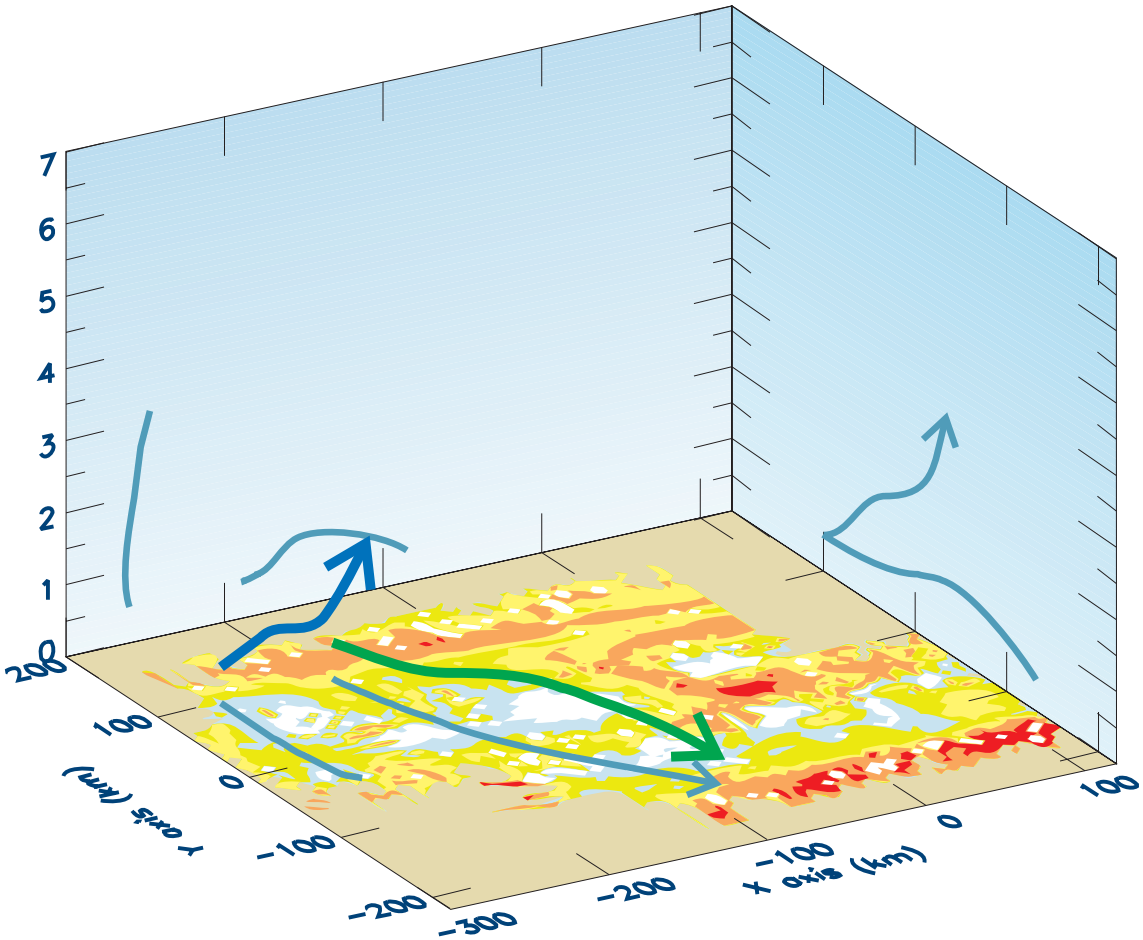

Figure 6.8: *Air parcel trajectory representative of the northerly flow: (a) westernmost trajectory (blue stream), (b) easternmost trajectory (green strem).*

tence of a vertical vorticity maximum in the DS region of the dry slot. This maximum extends vertically up to 3 km, with a peak magnitude of 6×10^{-4} s^{-1}. Another vertical cross-section (given in Fig. 6.6c) taken accross the cloud head, the dry intrusion and the main baroclinic zone cloud band (almost perpendicular to the cross-section of Fig. 6.6b) also indicates the strong link between the vertical vorticity maximum and the dry slot region DS. Unfortunately, the lack of radar targets (precipitating particles) in the upper-levels, and in particular in the dry slot region, does not allow documentation of an upper-level vorticity anomaly and its potential baroclinic interaction with the low-level vorticity anomaly seen in Figs. 6.6bc. This problem will be overcome in the future using analysis methods that combine Doppler radar and dropsonde information so as to access dynamic fields in both regions of clear-air and precipitation (Montmerle and Lemaître 1998; Bouniol et al. 1999).

6.6 Mass fields anomalies

The "virtual cloud" potential temperature and pressure perturbations at the 1.5-km altitude are given in Figs. 6.9a and 6.9b, respectively. Let us recall that these fields are deviations from a reference state that is constant horizontally, as discussed in Protat et al. (1998). Hence, these deviations include both the baroclinic basic state of the atmosphere and all other local horizontal perturbations developing from this basic state (such as warming or cooling associated with upright or slantwise motions). The temperature perturbation field (Fig. 6.9a) reveals a well-defined baroclinic signature from the colder northerly flow (left side of the domain) to the warmer W2, cold conveyor belt, and WCB flows (right side of the domain), with characteristic averaged horizontal temperature gradients of 9 K for 100 km accross the domain. This global baroclinic tendency is found to be modulated in precipitating areas by local diabatic warming, for instance on the southwestern border of the domain. However, it is to be noted that those local effects are likely not well-resolved, due to the fact that small-scale features are filtered out by the analysis for this mesoscale retrieval. Again, the effect of the diabatic processes on the mesoscale circulation will be addressed in a near-future by performing dynamic retrievals at convective-scale in these particular precipitating regions.

The pressure perturbation field (Fig. 6.9b) evidences a local minimum, characterized by mean horizontal gradients of roughly 6 mbar for 100 km. This pressure perturbation minimum is located along the easternmost baroclinic region of Fig. 6.9a, in the particular precipitating region A source of vertical transport to the southeast within the cyclone illustrated in Fig. 6.7b (W2 flow). Since these slantwise transports depend on latent heat release, this indicates that latent heat release likely plays a significant role in the secondary cyclone growth. This seems to support observationally the conclusions of Shutts (1990) deduced from a fine-mesh numerical simulation of a secondary cyclone, according to which the contribution of latent heat release to an explosive development appears to dominate the dry baroclinic instability process.

The location of the low pressure can be compared with the location of the vertical vorticity maximum at mesoscale. For this purpose, a horizontal cross-section of vertical vorticity at the 1.5-km altitude is given in Fig. 6.10. It exhibits a tongue of positive vertical vorticity oriented along the northeastern border of the northerly flow, characterized by two local maxima. The first maximum is located into the region of vertical mass transport to the northwest (described previously, Fig. 6.7a), and the second maximum is associated with the clear-air region DS. Comparison between Figs. 6.9b and 6.10 shows that the low pressure is slightly shifted on the southeastern border of the vertical vorticity core.

Pressure perturbation field at the 1.5-km altitude resulting only from the Coriolis terms (that is, using only accelerations due to the Coriolis and pressure forces in the two horizontal projections of the momentum equations) has been computed. First, let us notice the good agreement between the absolute wind field given in Fig. 6.6 and the "Coriolis-derived" pressure perturbation, with the horizontal wind that follows the pressure isolines, as expected. Comparison between this "Coriolis-derived" pressure perturbation and the retrieved "full" pressure perturbation field of Fig. 6.9b reveals the important contribution of other physical mechanisms than the Coriolis effect in the low pressure formation. It reveals in particular the southeastward shift of the low pressure (between the "full" and "Coriolis-derived" pressure fields). This low pressure lies on the southern border of the DS region, which suggests the importance of non-hydrostatic effects linked to the ascent of W2 and the reascent of the dry intrusion while approaching the cyclone center.

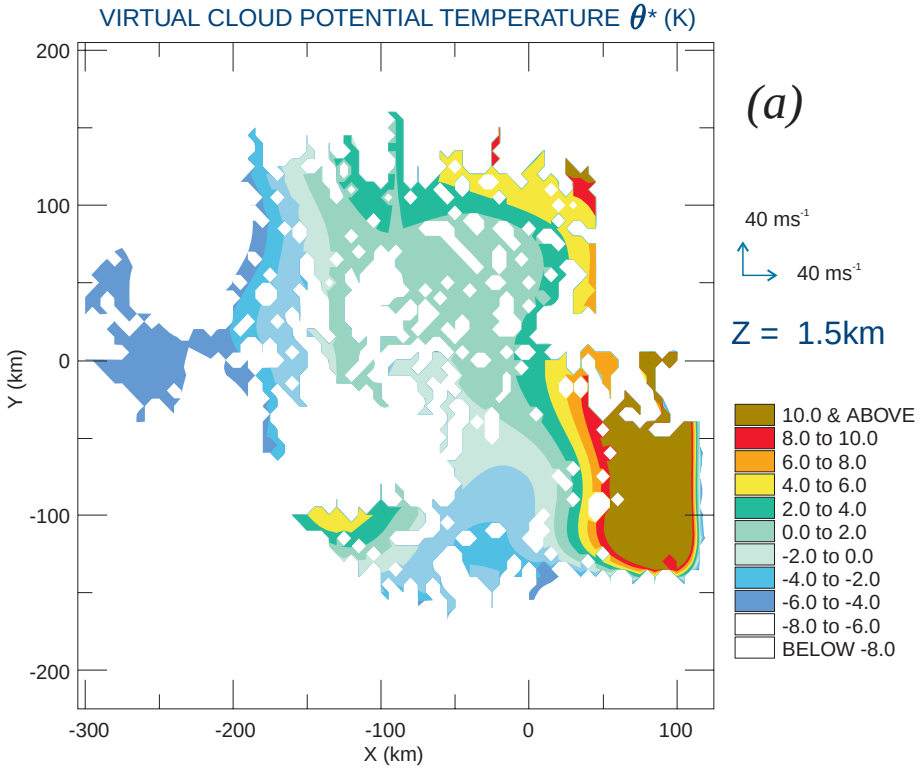

Figure 6.9: *"Virtual cloud" potential temperature (a) and pressure (b) perturbations at the 1.5 km altitude derived from the 3D wind field.*

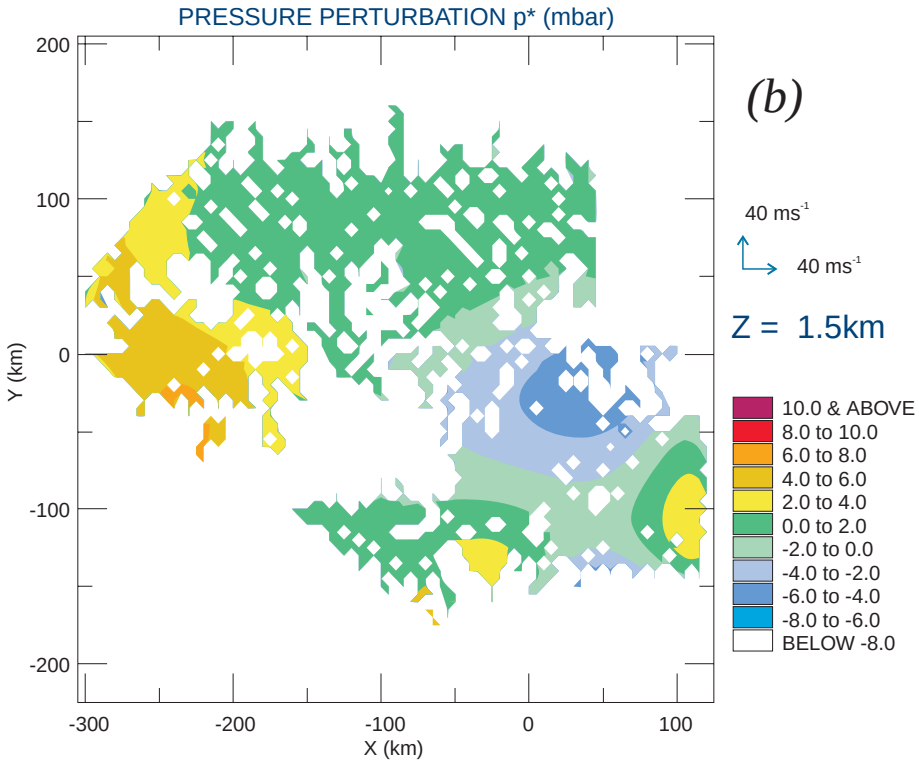

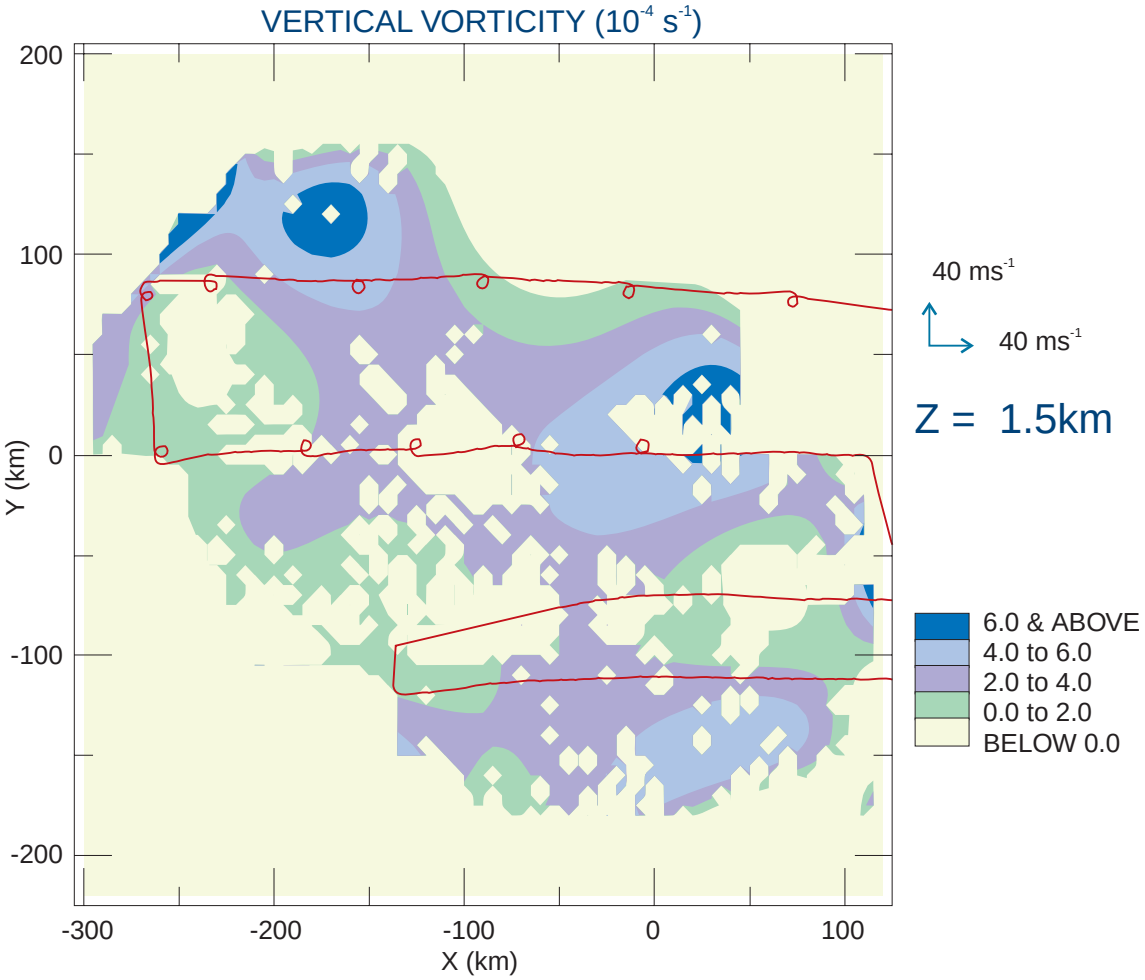

Figure 6.10: *Horizontal cross-section of vertical vorticity at the altitude of 1.5 km.*

6.7 Summary and perspectives

In this paper, the mesoscale dynamics of an explosively deepening secondary cyclone sampled during the field phase of FASTEX (IOP 12) was documented using airborne Doppler radar data. Let us recall that the meteorological interest of this case lies in the presence of well-developed cloud head and dry slot features and of a well-organized line of thunderstorms which highlights the interest to scrutinize the mesoscale dynamic structure of this particular case study. This study illustrates that the sampling strategy defined for FASTEX is suitable for accessing the mesoscale dynamics of the whole core of a cyclone, in addition to the internal structure of each precipitation component of this cyclone (as done more classically).

The main flows responsible for the mesoscale organization of the cyclone have been documented under the assumption of stationarity. First, this study confirms observationally the existence of a warm airflow W2 peeled-off from the base of the WCB and its crucial importance on the development of the most active part of the cloud head (in terms of precipitation), as claimed at broader scale by Browning and

Roberts (1994, 1996). It also evidences the intrusion of a dry airflow approaching the cyclone center. Unfortunately, the lack of radar targets (precipitating particles) in the upper-levels, and in particular in the dry slot region, does not allow documentation of an upper-level vorticity anomaly and its potential baroclinic interaction with the low-level vorticity anomaly.

A cold conveyor belt is found to contribute to the upward mass transport towards the upper part of the main baroclinic zone cloud band. Documentation of the distinct behaviour of the W2 and cold conveyor belt flows that feed distinct precipitating entities of the cyclone was not made possible using the present mesoscale 3-D fields, due to the limited areal coverage of the Doppler observations. These last two problems will be overcome in the near-future by combining Doppler radar data, dropsonde measurements, and numerical model outputs in order to access dynamic fields in both regions of clear-air and precipitation (Montmerle and Lemaître 1998; Bouniol et al. 1999) and to quantify the importance of the large-scale environmental forcing with respect to the mesoscale and convective-scale processes.

In addition, this study evidences a slight shift between the location of the high vertical vorticity core associated with the most active part of the cloud head and the location of the low pressure, suggesting the importance of the non-hydrostatic effects associated with the ascent of the peeled-off W2 flow and with the reascent of the dry intrusion while approaching the cyclone center. A further quantification of these non-hydrostatic processes will be conducted in a future paper by performing convective-scale retrievals in the low pressure area. The dynamical importance of a cold northerly flow which tends to wrap around the low center is also revealed by analysis of the mesoscale fields. It is suggested that the associated precipitating entities are generated by release of convective instability during the propagation of this flow above the warmer ocean. To confirm this aspect, a smaller-scale study of the air-sea interactions in this northerly flow area will be performed.

This paper highlights the high-quality of the IOP12 airborne Doppler dataset. It also shows the need to combine in the near-future airborne Doppler radar and dropsonde measurements in order to access multiscale processes involved in the mature stage of this FASTEX cyclone in both clear-air and precipitating regions and to address the numerous open questions raised by the present mesoscale study. This work is presently under progress (see recent results of Bouniol et al. 1999 concerning the FASTEX IOP16) using an analysis method that permits combination of such measurements (Montmerle and Lemaître 1998). The mesoscale fields analyzed in this paper will be used to initialize mesoscale models (see recent works of Montmerle 1998) in order to diagnose associated microphysical fields and evaluate the importance of microphysical processes in the cyclone organization. This advanced part of the interpretation is included in the *FASTEX Cloud System Study* project, also supported by the European Commission.

6.8 References

Appenzeller, C., 1994 :
Wave developments on surface fronts and stratospheric intrusions.
PhD thesis, Swiss Federal Institute of Technology (ETH). Dissertation No 10471, 117pp.

Baehr, C., B. Pouponneau, F. Ayrault, and A. Joly, 1999 :
Dynamical characterization and summary of the FASTEX cyclogenesis cases.
Quart. J. Roy. Meteor. Soc., *submitted.*

Bouniol, D., A. Protat, and Y. Lemaître, 1999 :
Mesoscale dynamics of a deepening secondary cyclone (FASTEX IOP16) : Three-dimensional structure retrieved from dropsonde data.
Quart. J. Roy. Meteor. Soc., *submitted.*

Browning, K. A., 1994 :
GEWEX Cloud System Study (GCSS) : Science Plan.
Volume **11**, IGPO Publication Series. 62 pp.

Browning, K. A, and N. M. Roberts, 1994 :
Structure of a frontal cyclone.
Quart. J. Roy. Meteor. Soc., **120**, 1535-1557.

Browning, K. A, and N. M. Roberts, 1996 :
Variation of precipitation structure along a cold front.
Quart. J. Roy. Meteor. Soc., **122**, 1845-1872.

Bond, N. A., and Co-authors, 1997:
The Coastal Observation and Simulation with Topography (COAST) experiment.
Bull. Amer. Meteor. Soc., **78**, (9), 1941-1955.

Bottger, H., M. Eckardt, and U. Katergiannakis, 1975 :
Forecasting extratropical storms with hurricane intensity using satellite information.
J. Appl. Meteorol., **14**, 1259-1265.

Carlson, T. N., 1980 :
Airflow through midlatitude cyclones and the comma cloud pattern.
Mon. Wea. Rev., **108**, 1498-1509.

Chaigne, E., 1998 :
Application de l'inversion du tourbillon potentiel (Aplication of the PV inversion technique).
Master's thesis, Ecole Nationale de la Météorologie, Note de Travail No 618, Toulouse, 86pp.

Dou, X. K., G. Scialom, and Y. Lemaître, 1996:
MANDOP analysis and airborne Doppler radar for mesoscale studies.
Quart. J. Roy. Meteor. Soc., **122**, 1231-1261.

Green, J. S. A., F. H. Ludlam and J. F. R. McIlveen, 1966 :
Isentropic relative-flow analysis and the parcel theory.
Quart. J. Roy. Meteor. Soc., **92**, 210-219.

Harrold, T. W., 1973 :
Mechanisms influencing the distribution of precipitation within baroclinic disturbances.
Quart. J. Roy. Meteor. Soc., **99**, 232-251.

Joly, A., D.Jorgensen, M.A.Shapiro, A.Thorpe, P.Bessemoulin, K.A.Browning, J.P.Cammas, J.P.Chalon, S.A.Clough, K.A.Emanuel, L.Eymard, R.Gall, P.H.Hildebrand, R.H.Langland, Y.Lemaitre, P.Lynch, J.A.Moore, P.O.G.Persson, C.Snyder, R.M.Wakimoto, 1997:
The Fronts and Atlantic Storm-Track Experiment (FASTEX): Scientific Objectives and Experimental Design.
Bull. Amer. Meteor. Soc., **78**, (9), 1917–1940.

Joly, A., K.A. Browning, P. Bessemoulin, J.P. Cammas, G. Caniaux, J.P. Chalon, S.A. Clough, R. Dirks, K.A. Emanuel, L. Eymard, R. Gall, T.D. Hewson, P.H. Hildebrand, D. Jorgensen, F. Lalaurette, R.H. Langland, Y. Lemaitre, P. Mascart, J.A. Moore, P.O.G. Persson, F. Roux, M.A. Shapiro, C. Snyder, Z. Toth, and R.M. Wakimoto, 1999:
Overview of the field phase of the Fronts and Atlantic Storm-Track Experiment (FASTEX) project.
Quart. J. Roy. Meteor. Soc., **125**, *submitted.*

Jorgensen D.P., P. Bessemoulin, S. Clough, and J.A. Moore.
Fastex operations plan, 1996.
Technical Report 5, FASTEX Project Office, Centre National de Recherches Météorologiques, 164pp.

Lemaître, Y., and A. Protat, 1998 :
Dynamics of a "bomb-like" deepening secondary cyclone from airborne Doppler radar.
Quart. J. Roy. Meteor. Soc., *under revision.*

Lemaître, Y., A. Protat and D. Bouniol, 1999:
Pacific and Atlantic "bomb-like" deepening in mature phase: a comparative study.
Quart. J. Roy. Meteor. Soc., *submitted.*

Montmerle, T., and Y. Lemaître, 1998 :
Three-dimensional variational data analysis to retrieve thermodynamical and dynamical fields from various nested measurements.
J. Atmos. Oceanic Technol, **15**, 360-379.

Montmerle, T., 1998 :
Validation et initialisation d'un modèle tridimensionnel méso-échelle non-hydrostatique par des données expérimentales issues de l'expérience TOGA-COARE (Validation and initialization of a 3-D non-hydrostatic mesoscale model using data collected during the TOGA-COARE experiment).
PhD thesis, University Paris 6. Available from the author, 10-12 Avenue de l'Europe, 78140 Vélizy, France.

Neiman, P. J. , and M. A. Shapiro, 1993 :
The life cycle of an extratropical marine cyclone. Part I : Frontal-cyclone evolution and thermodynamic air-sea interaction.
Mon. Wea. Rev., **121**, 2153-2176.

Protat, A., Y. Lemaître, and G. Scialom, 1997:
Retrieval of kinematic fields using a single-beam airborne Doppler radar performing circular trajectories.
J. Atmos. Oceanic Technol., **14**, 769-791.

Protat, A., Y. Lemaître, and G. Scialom, 1998 :
Thermodynamic analytical fields from Doppler radar data by means of the MANDOP analysis.
Quart. J. Roy. Meteor. Soc., **124**, 1633-1669.

Reed, R. J., and E. F. Danielsen, 1959 :
Fronts in the vicinity of the tropopause.
Arch. Meteorol. Geophys. Bioklim., **A11**, 1-17.

Sanders, F., and J. R. Gyakum, 1980 :
Synoptic-dynamic climatology of the 'bomb'.
Mon. Wea. Rev., **108**, 1589-1606.

Scialom, G. and Y. Lemaître, 1990 :
A new analysis for the retrieval of three-dimensional mesoscale wind fields from multiple Doppler radar.
J. Atmos. Oceanic Technol., **7**, 640-665.

Scialom, G., A. Protat, and Y. Lemaître, 1999 :
Vertical structure of a FASTEX secondary cyclone derived from dual-beam airborne radar data.
Quart. J. Roy. Meteor. Soc., *submitted.*

Shutts, G. J., 1990 :
Dynamical aspects of the October storm, 1987 : A study of a successful fine-mesh simulation.
Quart. J. Roy. Meteor. Soc., **116**, 1315-1347.

Vallis, G. K., G. J. Shutts, and M. E. B. Gray, 1997 :
Balanced mesoscale motion and stratified turbulence forced by convection.
Quart. J. Roy. Meteor. Soc., **123**, 1621-1652.

Young, M. V., 1989 :
Investigation of a cyclogenesis event, 26-29 July 1988, using satellite imagery and numerical model diagnostics.
Meteorol. Mag., **118**, 185-196.

Young, M. V., G. A. Monk, and K. A. Browning, 1987 :
Interpretation of satellite imagery of a rapidly deepening cyclone.
Quart. J. Roy. Meteor. Soc., **113**, 1089-1115.